

## Supporting Information

### Proton Conduction in 2D Aza-Fused Covalent Organic Frameworks

Zheng Meng,<sup>1</sup> Aylin Aykanat,<sup>1</sup> Katherine A. Mirica\*

<sup>1</sup>*Department of Chemistry, Burke Laboratory, Dartmouth College, Hanover, NH 03755*

\*E-mail: Katherine.A.Mirica@dartmouth.edu

#### Content

<b>1. Materials and Methods</b> .....	S2
<b>2. Synthesis of the aza-Fused <math>\pi</math>-Conjugated COFs</b> .....	S2
<b>2.1. Synthesis of aza-COF-1</b> .....	S2
<b>2.2. Synthesis of aza-COF-2</b> .....	S3
<b>2.3. Synthesis of H<sub>3</sub>PO<sub>4</sub> Acidified COFs aza-COF-1<sub>H</sub> and aza-COF-2<sub>H</sub></b> .....	S3
<b>3. ATR-FTIR Spectroscopy</b> .....	S3
<b>4. X-ray Photoelectron Spectroscopy</b> .....	S6
<b>5. Elemental Analysis</b> .....	S8
<b>6. Powder X-ray Diffraction</b> .....	S9
<b>7. Structural Analysis</b> .....	S13
<b>8. SEM and TEM</b> .....	S14
<b>9. Brunauer–Emmett–Teller (BET) Analysis</b> .....	S19
<b>10. Thermal Gravimetric Analyses (TGA)</b> .....	S21
<b>11. Measurements of Proton Conductivity</b> .....	S22
<b>12. Summary of the COFs Based Proton Conducting Materials</b> .....	S28
<b>13. References</b> .....	S29

## 1. Materials and Methods

Hexaketocyclohexane octahydrate (CAS N.O.: 527-31-1), 1,2,4,5-benzenetetramine tetrahydrochloride (CAS N.O.: 4506-66-5), sulfuric acid (98%, CAS N.O.: 7664-93-9) and phosphoric acid (85 wt. % in H<sub>2</sub>O, CAS N.O.: 7664-38-2) were purchased from Sigma Aldrich. Acetone (CAS N.O.: 67-64-1), methanol (CAS N.O.: 67-56-1) and *N,N*-dimethylformamide (CAS N.O.: 68-12-2) were purchased from BDH Chemicals. 1,3-Dimethyl-2-imidazolidinone (CAS N.O.: 80-73-9), *N*-methyl-2-pyrrolidone (CAS N.O.: 872-50-4) were purchased from TCI America. Compounds 2,3,6,7,10,11-hexaaminotriphenylene hexahydrochloride were synthesized according to the literature procedures.<sup>S1</sup>

Scanning Electron Microscopy (SEM) and Energy Dispersive X-ray Spectroscopy (EDX) were performed using a Hitachi TM3000 SEM (Tokyo, Japan) equipped for X-ray microanalysis with a Bruker Edax light element Si(Li) detector (Billerica, MA). Transmission electron microscopy was carried out at a Tecnai F20ST FEG TEM instrument. Powder X-ray diffraction (PXRD) measurements were performed with a Rigaku sixth generation MiniFlex X-ray diffractometer with a 600 W (40 kV, 15 mA) CuK $\alpha$  ( $\lambda = 1.54 \text{ \AA}$ ) radiation source. Ivium CompactStat B31250 potentiostat was used for electrochemical measurements. Nitrogen adsorption experiments were performed with ASAP Plus 2020 (Micromeritics, Norcross, Georgia) instrument. Elemental analyses were performed by *Atlantic Microlab, Inc.* X-ray photoelectron spectroscopy experiments were conducted on Physical Electronics Versaprobe II X-ray Photoelectron Spectrometer under ultrahigh vacuum (base pressure  $10^{-10}$  mbar). The measurement chamber was equipped with a monochromatic Al (K $\alpha$ ) X-ray source. Both survey and high-resolution spectra were obtained using a beam diameter of 200  $\mu\text{m}$ . X-ray photoelectron spectroscopy (XPS) experiments were performed at the Center for Materials Science and Engineering at the Massachusetts Institute of Technology.

## 2. Synthesis of the aza-Fused $\pi$ -Conjugated COFs

### 2.1. Synthesis of aza-COF-1

2,3,6,7,10,11-Hexaaminotriphenylene hexahydrochloride (CAS N.O.: 1350518-27-2, 269 mg, 0.5 mmol) and hexaketocyclohexane octahydrate (156 mg, 0.5 mmol) were dissolved in 50 mL of 1,3-dimethyl-2-imidazolidinone (DMI). Ten drops of concentrated sulfuric acid (98%) were slowly added to the reaction mixture. The reaction flask was warmed to 60 °C for 4 h under N<sub>2</sub> atmosphere. After that the reaction was heated to 175 °C for 5 days. The flask was then cooled to room temperature, and the solid product was collected by vacuum filtration, and washed with

water (30 mL × 3) and acetone (30 mL × 5). The thus obtained materials (152 mg, yield 80 %) as purple brown powder were then used for powder X-ray diffraction, scanning electron microscopy, and transmission electron microscopy.

The resultant solid was further activated using a Soxhlet extractor with methanol for two days, and dried for 24 hours in a vacuum (20 mTorr) oven at 65°C. The activated material was then used for elemental analysis, x-ray photoelectron spectroscopy, gas adsorption measurements, and proton conduction test.

## 2.2. Synthesis of aza-COF-2

This synthetic procedure was adapted from V. Briega-Martos et al.<sup>S2</sup> using modified conditions. To a 25-mL round bottom flask containing 1,2,4,5-benzenetetramine tetrahydrochloride (426 mg, 1.5 mmol) and hexaketocyclohexane octahydrate (312 mg, 1.0 mmol) was added 10 mL of *N*-methyl-2-pyrrolidone (NMP) and ten drops of concentrated sulfuric acid (98%). The reaction mixture was then heated to 185 °C under N<sub>2</sub> atmosphere for 5 days. The black precipitate was filtrated and washed with water (30 mL × 3) and acetone (30 mL × 5) to give solid black powder (245 mg, yield 92 %) after being dried.

The material was further activated using a Soxhlet extractor with methanol for two days, and then dried for 24 hours in a vacuum (20 mTorr) oven at 65°C in preparation for elemental analysis, X-ray photoelectron spectroscopy, gas adsorption measurements, and proton conduction test.

## 2.3. Synthesis of H<sub>3</sub>PO<sub>4</sub> Acidified COFs aza-COF-1<sub>H</sub> and aza-COF-2<sub>H</sub>

To a round bottom flask containing 25 mL of 12 M H<sub>3</sub>PO<sub>4</sub> was added 100 mg of **aza-COF-1**. The suspension was stirred at 60 °C for four hours. The solid was then filtered, washed with water (50 mL × 3), and vacuum dried at 65 °C for 2 days.

A similar procedure was used for the acidification of **aza-COF-2** to generate **aza-COF-2<sub>H</sub>**.

## 3. ATR-FTIR Spectroscopy

Infrared spectra were collected using a JASCO model FT IR-6100 Fourier transform infrared spectrophotometer. Attenuated total reflection Fourier-transform infrared (ATR-FTIR) spectrum of **aza-COF-1** showed the disappearance of the vibrational bands due to the NH<sub>2</sub> groups of HATP•6HCl (3417 and 3333 cm<sup>-1</sup>) and the C=O group of HKH•8H<sub>2</sub>O (1663 cm<sup>-1</sup>), and the appearance of bands at 1514, 1442, and 1389 cm<sup>-1</sup>, confirming

the formation of phenazine linkages (**Figure S1**).<sup>S3</sup> Analogous changes were also found in **aza-COF-2**, where the bands characteristic of starting materials at 2892  $\text{cm}^{-1}$  ( $-\text{NH}_2$ ) and 1663  $\text{cm}^{-1}$  ( $\text{C}=\text{O}$ ) disappeared and strong bands at 1439, 1220  $\text{cm}^{-1}$  ascribed to the  $\text{C}=\text{C}$  and  $\text{C}=\text{N}$  stretching in pyrazine rings (**Figure S2**) emerged.<sup>S4-5</sup>

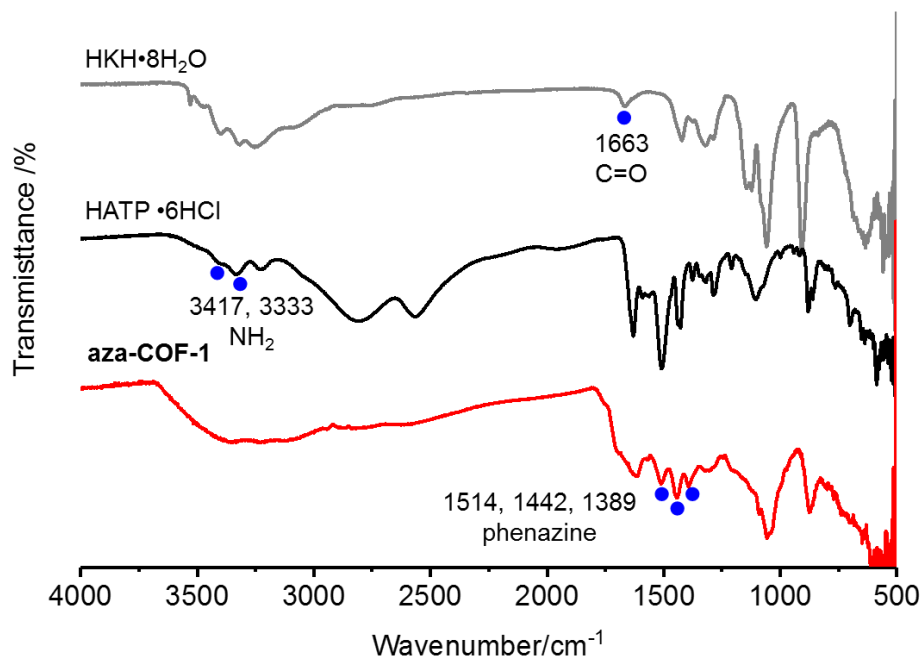


**Figure S1.** Comparison of ATR-FTIR spectra of HKH·8H<sub>2</sub>O, HATP·6HCl and aza-COF-1.

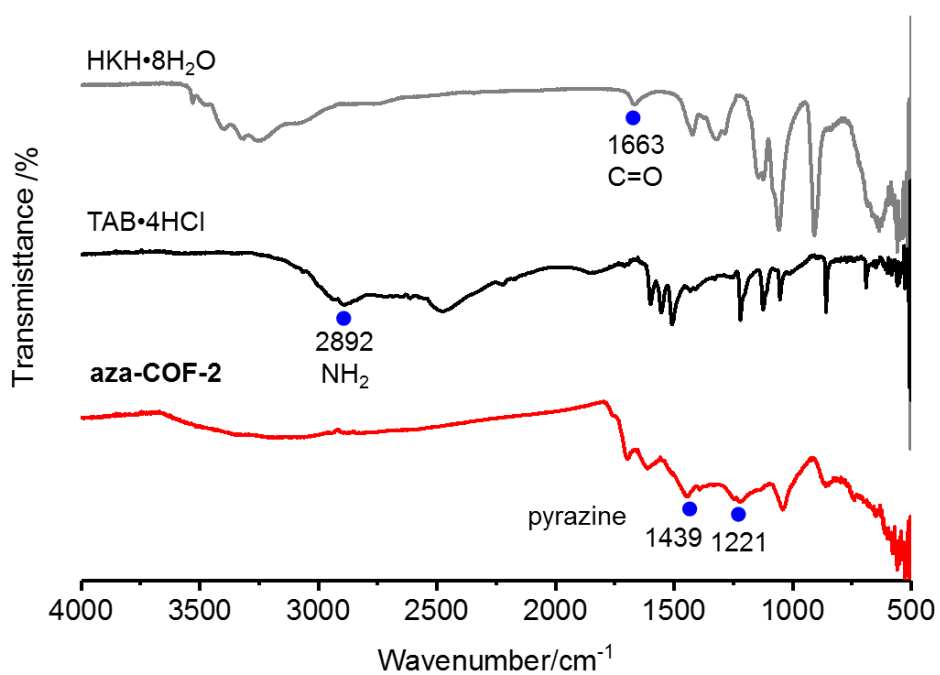


**Figure S2.** Comparison of ATR-FTIR spectra of HKH•8H<sub>2</sub>O, TAB•4HCl and aza-COF-2.

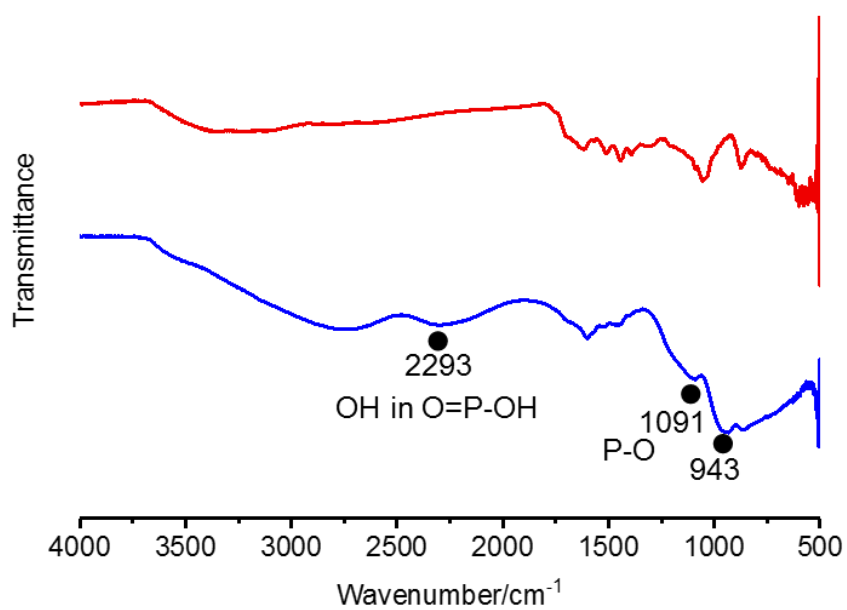


**Figure S3.** ATR-FTIR spectra of aza-COF-1 before (red) and after (blue) H<sub>3</sub>PO<sub>4</sub> acidification.

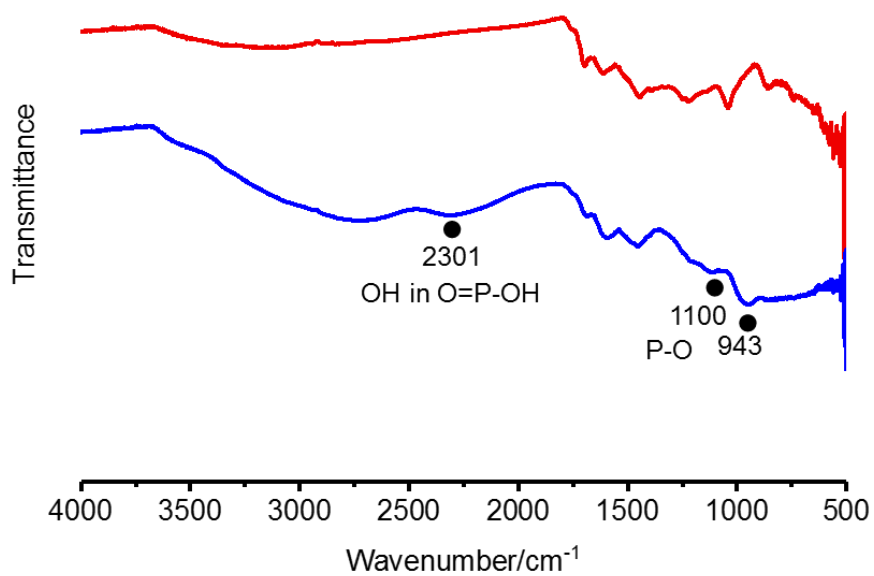


**Figure S4.** ATR-FTIR spectra of aza-COF-2 before (red) and after (blue) H<sub>3</sub>PO<sub>4</sub> acidification.

## 4. X-ray Photoelectron Spectroscopy

X-ray photoelectron spectroscopy (XPS) experiments were conducted on a Physical Electronics Versaprobe II X-ray Photoelectron Spectrometer under ultrahigh vacuum (base pressure  $10^{-10}$  mbar). The measurement chamber was equipped with a monochromatic Al ( $K\alpha$ ) X-ray source. Both survey and high-resolution spectra were obtained using a beam diameter of 200  $\mu\text{m}$ . The spectra were processed with CasaXPS.

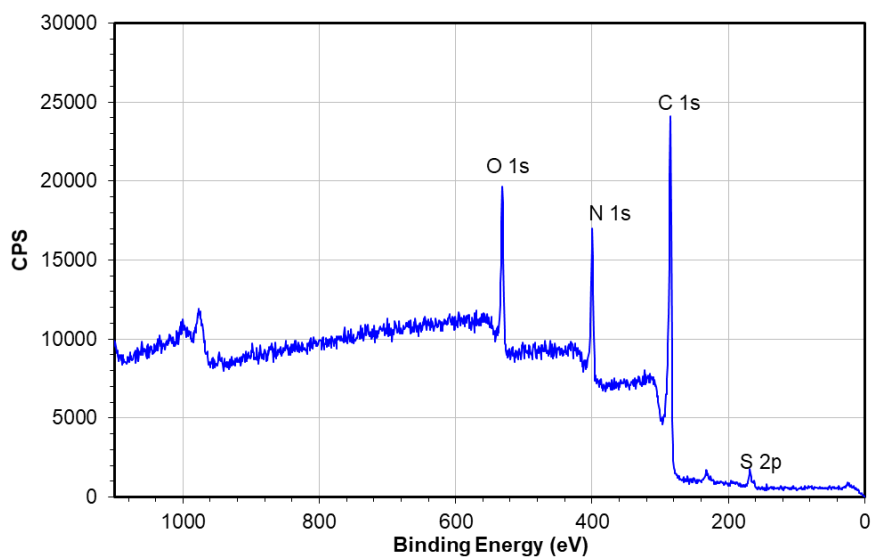


**Figure S5.** XPS survey spectrum showing C, N, O and a slight amount of S in **aza-COF-1**.

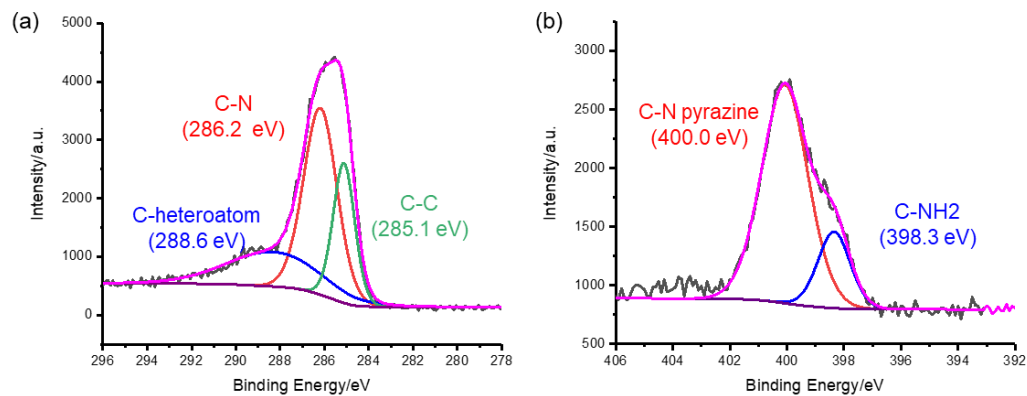


**Figure S6.** Deconvoluted XPS spectra of the **aza-COF-1**: (a) C 1s; (b) N 1s. The black curve represents original data while the pink curve is the sum of different deconvoluted peaks. In (a), the green curve is due to C1s C=C and the red curve corresponds to C1s C=N. In (b) red curve corresponds to N1s C=N.

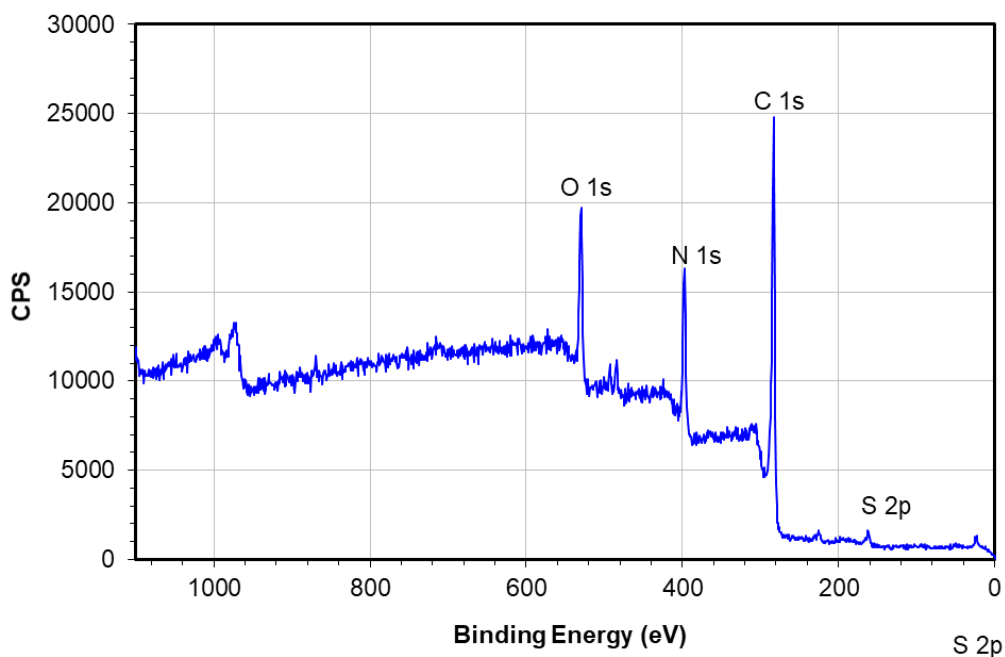


**Figure S7.** XPS survey spectrum showing C, N, O and a small amount of S in **aza-COF-2**.

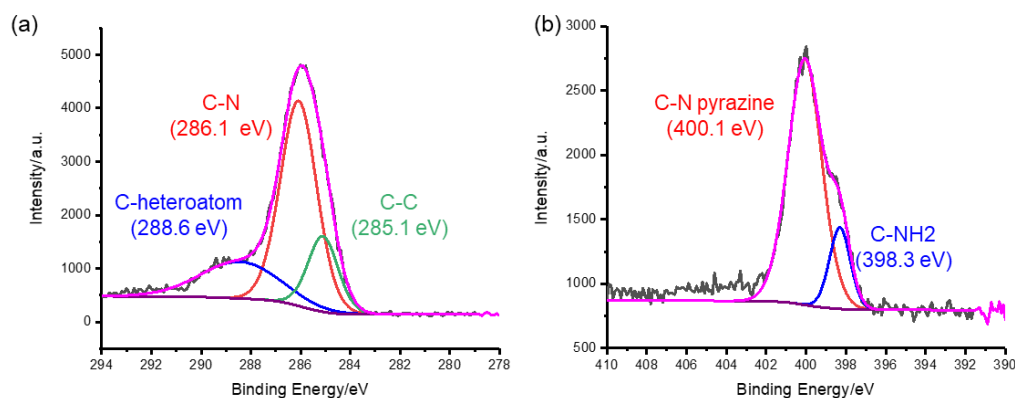


**Figure S8.** Deconvoluted XPS spectra of the **aza-COF-2**: (a) C 1s; (b) N 1s. The black curve represents original data and the pink curve is the sum of the different deconvoluted peaks. In (a) the green curve corresponds to C1s C=C and the red curve corresponds to C1s C=N. In (b) the red curve corresponds to N1s C=N.

The XPS spectra revealed the presence of abundant C and N in both **aza-COF-1** and **aza-COF-2**. The corresponding C and N contents are 73% and 15% for **aza-COF-1**, and 71% and 16% for **aza-COF-2** suggested by the XPS analysis (**Figure S5, S7**). Small amount (~3%) of S element was also observed in **aza-COF-1**, which is similar with the result from the elemental analysis. XPS showed characteristic band for the K-edge of carbon (286 eV) and nitrogen (400 eV) in C=N bond (**Figure S5-S8**), indicating the presence of  $sp^2$ -hybridized nitrogen atoms.

Deconvolution of High-resolution scans of the C1s spectrum showed three peaks with binding energies of 285.1, 286.2 and 288.6 eV, which can be respectively ascribed to the C=C, C=N and other heteroatom linked carbon. Deconvolution of High-resolution scans of the N1s spectrum revealed two peaks, corresponding to the two different N in C-NH<sub>2</sub> and C-N<sub>pyrazine</sub> respectively. The relative amount of the nitrogen in -NH<sub>2</sub> in **aza-COF-1** and **aza-COF-2** are 19% and 15%, respectively. We attribute the presence of the -NH<sub>2</sub> mainly due to the -NH<sub>2</sub> residue at the edges of two-dimensional sheet. The presence of edge group (-NH<sub>2</sub> and -C=O) were also observed in the nitrogenated holey two-dimensional C<sub>2</sub>N crystals reported by Beak's group, which can be thermally stripped of at a high temperature.<sup>S6</sup> Both XPS and elemental analysis (See below, **Table S1-S2**) suggested the presence of a small amount (~2% by XPS and 0.9% by elemental analysis) of sulfur within the structure of **aza-COF-1**, which can be attributed to residual sulfuric acid introduced during synthesis, despite the rigorous activation of the material by using methanol in a Soxhlet extractor for two days.

## 5. Elemental Analysis

Elemental analyses, including C, H, N and S, were performed by Atlantic Microlab inc. using combustion method by automatic analyzers. The results are listed below. The elemental analysis showed difference between the experimental and theoretical values. This difference can be at least from two aspects. Firstly, due to the porous characteristic of the materials, small molecules (moisture, oxygen, and etc.) can be encapsulated by the COFs. Secondly, the as synthesized materials may contain unreacted amino group and carbonyl groups on the edges of the crystallites of the materials because of the undesired termination of the condensation reaction.<sup>S6</sup> We found that in the elemental analysis the weight ratio of C/N in **aza-COF-1** (3.53) and **aza-COF-2** (2.21) are in better agreement with their theoretical ratios (3.43 and 2.14, respectively, See **Table S1-S2**).

**Table S1.** Elemental analysis of **aza-COF-1**.

<i>Sample</i>	<b>Element</b>	<b>Theoretical<sup>1</sup></b>	<b>Theoretical<sup>2</sup></b>	<b>Found</b>
<b>aza-COF-1</b>	C	76.19	59.26	59.36
	N	22.21	17.28	16.79
	H	1.60	3.73	3.87
	S	0	0	0.93

<sup>1</sup>Based on the formula C<sub>8</sub>H<sub>2</sub>N<sub>2</sub>. <sup>2</sup>Based on formula C<sub>8</sub>H<sub>2</sub>N<sub>2</sub>•2H<sub>2</sub>O in which every N atom in pyrazine unit binding to one H<sub>2</sub>O molecule.

**Table S2.** Elemental analysis of **aza-COF-2**.

<i>Sample</i>	<b>Element</b>	<b>Theoretical<sup>1</sup></b>	<b>Theoretical<sup>2</sup></b>	<b>Found</b>
<b>aza-COF-2</b>	C	67.42	56.08	54.87
	N	31.45	26.16	20.42
	H	1.13	2.82	3.86
	S	0	0	0

<sup>1</sup>Based on the formula C<sub>10</sub>H<sub>2</sub>N<sub>4</sub>. <sup>2</sup>Based on formula C<sub>8</sub>H<sub>2</sub>N<sub>2</sub>•2H<sub>2</sub>O in which every pyrazine unit binding to one H<sub>2</sub>O molecule.

## 6. Powder X-ray Diffraction

Powder X-ray diffraction (PXRD) data of **aza-COF-1** and **aza-COF-2** were collected on a Rigaku sixth generation MiniFlex X-ray diffractometer. Cu K $\alpha$  radiation ( $\lambda = 1.5406 \text{ \AA}$ ; 600 W, 40 kV, 15 mA) was focused using a planar Göbel mirror riding the K $\alpha$  line. In the PXRD spectrums, the peak intensities of [001] peaks are significantly higher than those of [100] in experimental spectra, which are much lower in the theoretical spectra.

The peak intensities of [001] peaks are significantly higher than those of [100] in experimental spectra, which should be much lower in the theoretical spectra. We noticed that the similar phenomenon has also been observed in structurally-related materials, like graphitic carbon nitride (*g*-C<sub>3</sub>N<sub>4</sub>)<sup>S7</sup> and C<sub>2</sub>N crystals.<sup>S6</sup> In the latter example, the [100] peak is not even visible and only [001] peak is shown. These results demonstrate the highly preferential stacking along *c* axis—the stacking of the conjugated aromatic system, in this type of layered materials. We think the preferential stacking of the 2D layers in these materials along *c* axis should be the reason for the relatively high intensities for [001] peaks. Morphology characterization of the pressed materials of **aza-COF-1<sub>H</sub>** and **aza-COF-2<sub>H</sub>** showed some objects with flat surface (**Figure S24, S26**), indicating that the pressure has impact on the stacking of the materials. The arrangement of the materials along the *c* direction could be further enhanced, which led to decrease in relative intensity of [100] peak (**Figure S11-S12**).

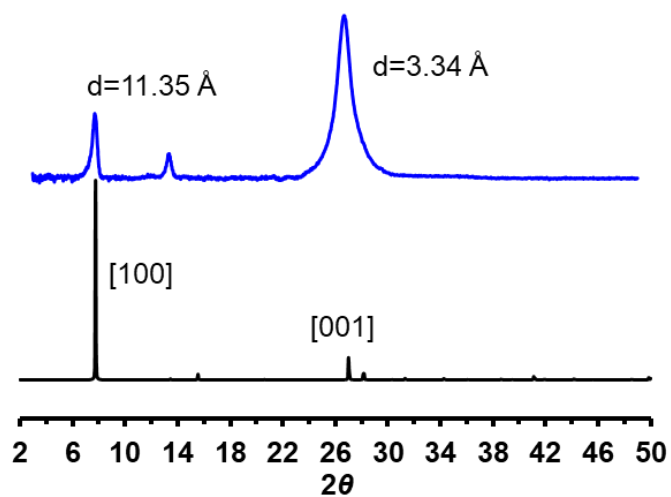


Figure S9. Experimental (blue line) and simulated PXRD pattern (black line) of **aza-COF-1**.

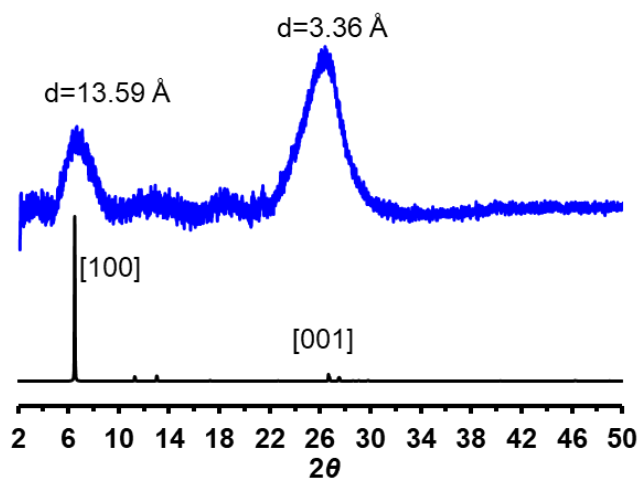
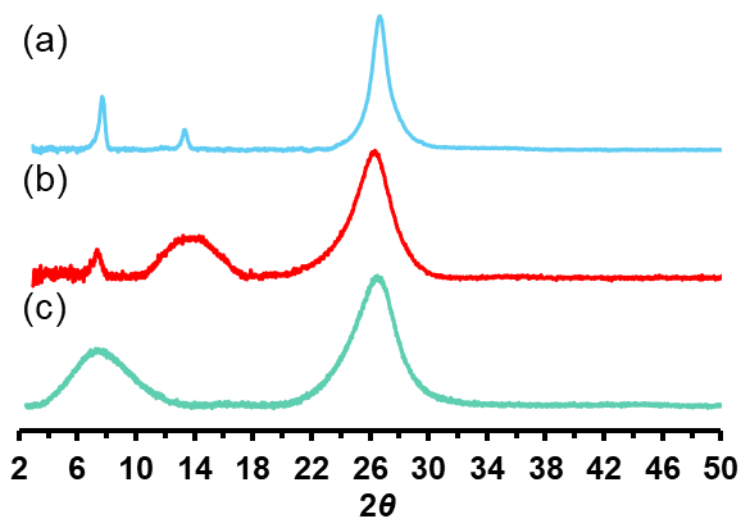
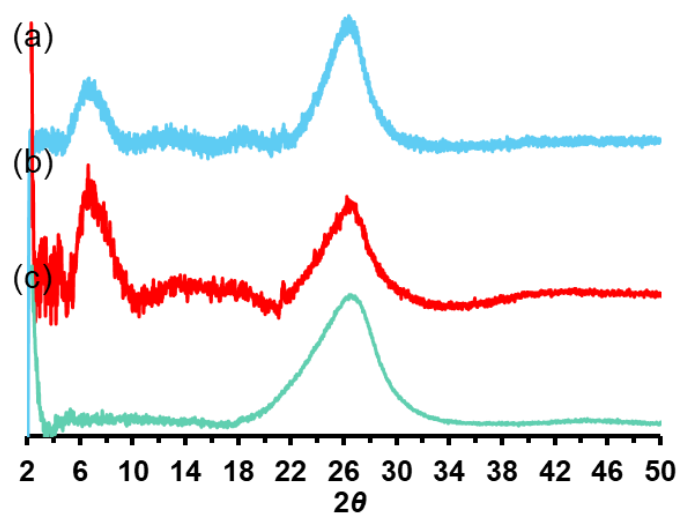


Figure S10. Experimental (blue line) and simulated PXRD pattern (black line) of **aza-COF-2**.



**Figure S11.** PXRD pattern of (a) **aza-COF-1**, (b) **aza-COF-1<sub>H</sub>** before being pressed, and (c) **aza-COF-1<sub>H</sub>** after being pressed into a pellet.



**Figure S12.** PXRD pattern of (a) **aza-COF-2**, (b) **aza-COF-2<sub>H</sub>** before being pressed, and (c) **aza-COF-2<sub>H</sub>** after being pressed into a pellet.

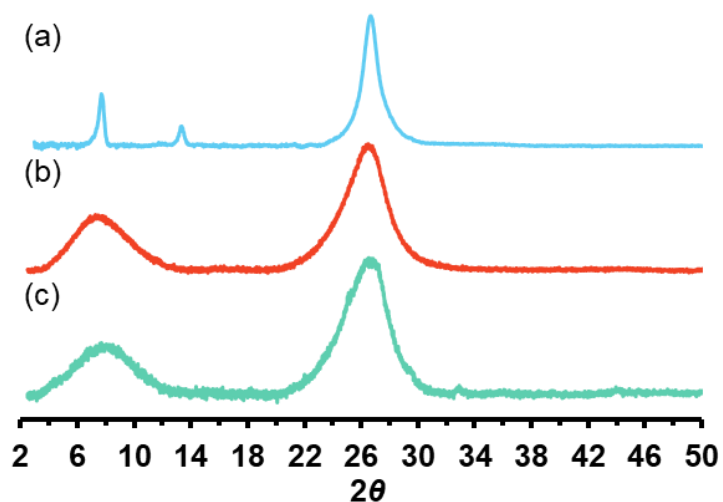


**Figure S13.** PXRD pattern of (a) aza-COF-1, (b) aza-COF-1 after treated with 12 M HCl for 24 hours, and (c) aza-COF-1 after treated with 14 M KOH for 24 hours.

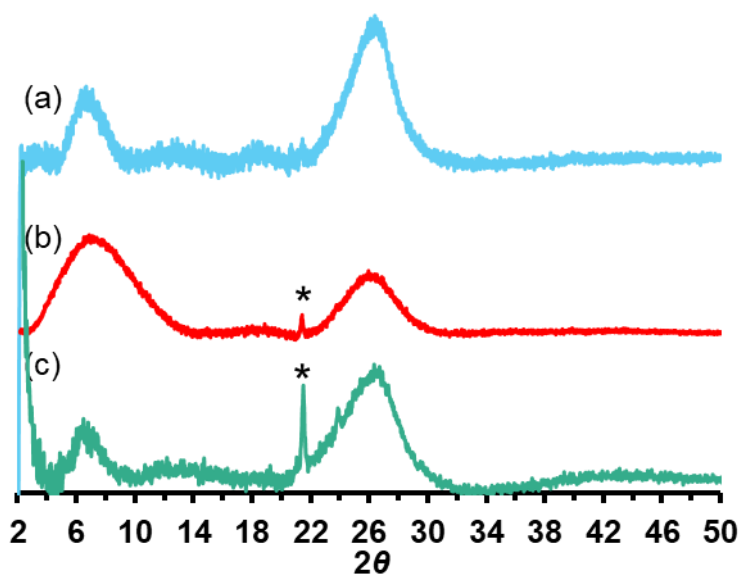


**Figure S14.** PXRD pattern of (a) aza-COF-2, (b) aza-COF-2 after treated with 12 M HCl for 24 hours, and (c) aza-COF-2 after treated with 14 M KOH for 24 hours. The peaks marked with \* are from the petroleum jelly that is used to attach the materials on the PXRD plate.

## 7. Structural Analysis

To generate the cell parameters of the two COFs, model structures which are hexagons supposed to form in the COFs, were built. These two hexagons were optimized by MM2 force field. The structures are shown in **Figure S15a** and **Figure S16a**.

Then optimized model structures were imported into Materials Studio and then converted into fractional coordinates using cell length  $a = b = 11.97 \text{ \AA}$  and  $a = b = 15.70 \text{ \AA}$ , respectively for **aza-COF-1** and **aza-COF-2**, which were determined from the corresponding model molecules. Interlayer spacing of 3.34, 3.36  $\text{\AA}$  were used for consistency with the PXRD signal. P-6m2 and P6/mmc symmetry were then respectively imposed into the unit cell of **aza-COF-1** and **aza-COF-2** with a threshold of 1.0 pm. The unit cell was then optimized in the CASTEP module using the PBE (Perdew-Burke-Ernzerhof) exchange-correlation functional. An energy cutoff of 500 eV and k-point mesh of  $2 \times 2 \times 6$  were used for the optimization. During structural relaxation, all atoms were relaxed until the forces were smaller than  $10^{-6}$  eV/atom. The optimized cell parameters for **aza-COF-1** and **aza-COF-2** shown in **Figure S15b** and **Figure S16b**, respectively.

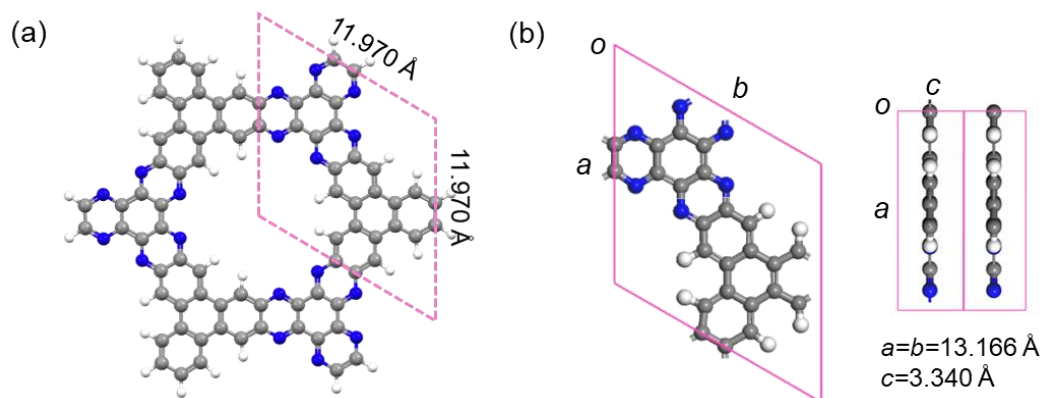


**Figure S15.** (a) Model complex for the generation of the cell parameter of **aza-COF-1**. (b) Unit cell of **aza-COF-1**.

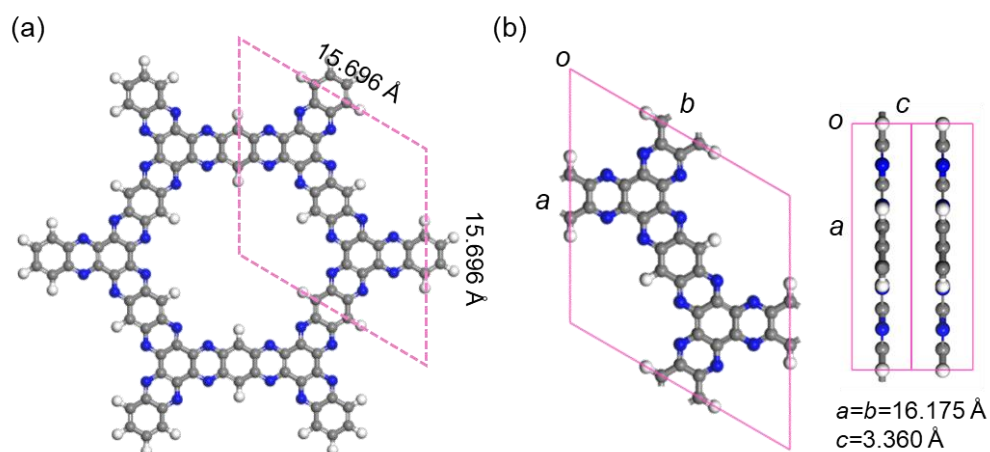


**Figure S16.** (a) Model complex for the generation of the cell parameter of **aza-COF-2**. (b) Unit cell of **aza-COF-2**.

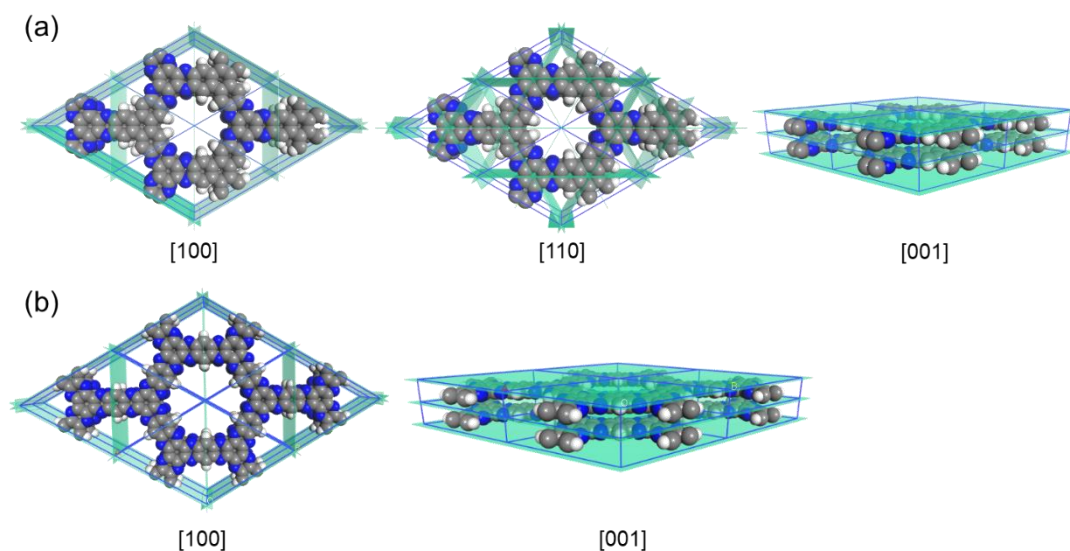


**Figure S17.** (a) Representation of the planes [100], [110] and [001] in the crystal structure of **aza-COF-1**, and (b) the [100] and [001] planes in the crystal structure of **aza-COF-2**.

## 8. SEM and TEM

Scanning electron microscopy of **aza-COF-1** and **aza-COF-2** were obtained using a Hitachi TM3000 SEM. The material was pressed onto carbon conductive tape that was attached to the aluminum plate. The images were taken at a 10 mm working distance using a 15 kV beamline in a  $10^{-6}$  Torr vacuum chamber.

Transmission electron microscopy was carried out in a Tecnai F20ST FEG TEM instrument. The sample was prepared by dropcasting an acetone suspension (0.5 mg in 5 mL) of aza-COF onto a copper grid (300 mesh, 3.0

mm O.D). An operating voltage of 120 kV was used for imaging.

The EDAX data for materials obtained by filtration and washing with water (30 mL  $\times$  3) and acetone (30 mL  $\times$  5), showed that there are C, N, O and S in **aza-COF-1** and that there are C, N, O, Cl and S in **aza-COF-2**. The S content may result from the use of the sulfuric acid as catalyst in the reaction. The Cl elemental likely originates from the 1,2,4,5-benzenetetramine tetrahydrochloride, which is one of the two building blocks used for the synthesis of **aza-COF-2**. The activation procedure involving washing of the material with methanol in a Soxhlet extractor for two days (see also **section 2**) can reduce the amount of the Cl and S related species in **aza-COF-2**, as evident from the XPS and elemental analysis (**Figure S7 and Table S2**). However, small amount of S element, was still found in **aza-COF-1** after the rigorous washing (**Table S1**). These results indicated that some small molecule impurities maybe present in pristine materials.

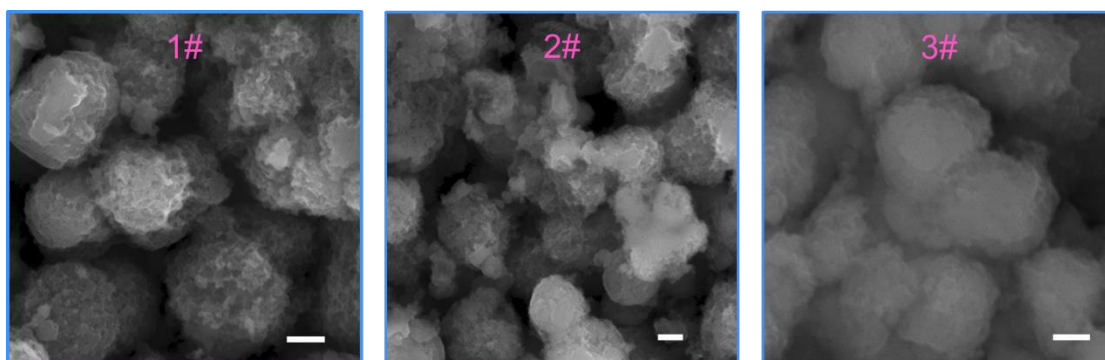


**Figure S18.** SEM images of **aza-COF-1** from three different batches of synthesis (scale bar: 500 nm).

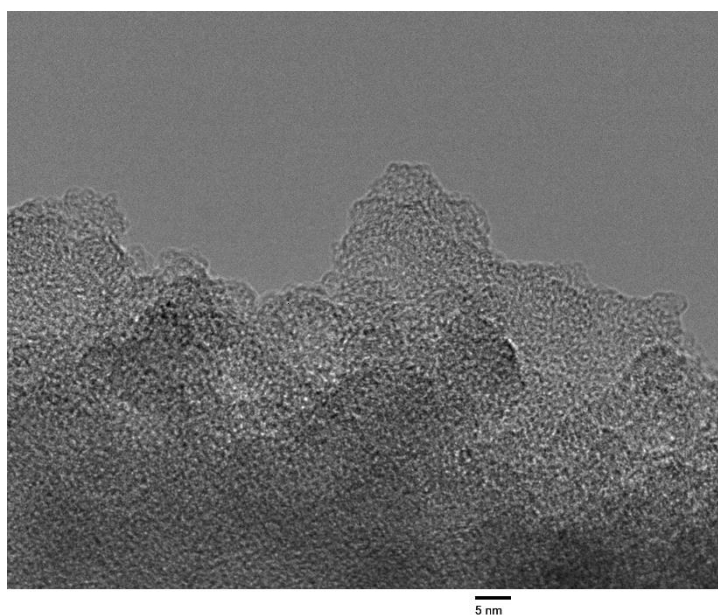


**Figure S19.** TEM image of **aza-COF-1**.

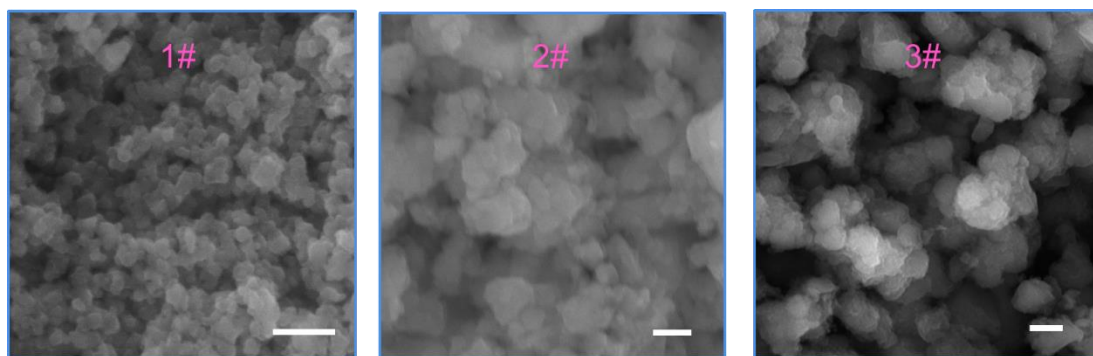


**Figure S20.** SEM images of **aza-COF-2** from three different batches of synthesis (scale bar: 500 nm).

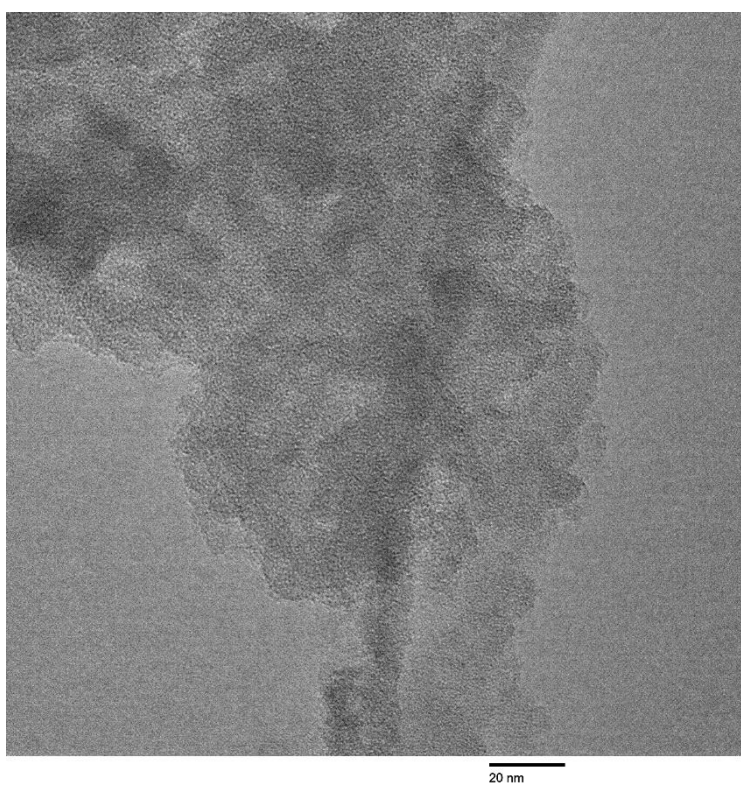


**Figure S21.** TEM image of **aza-COF-2**.

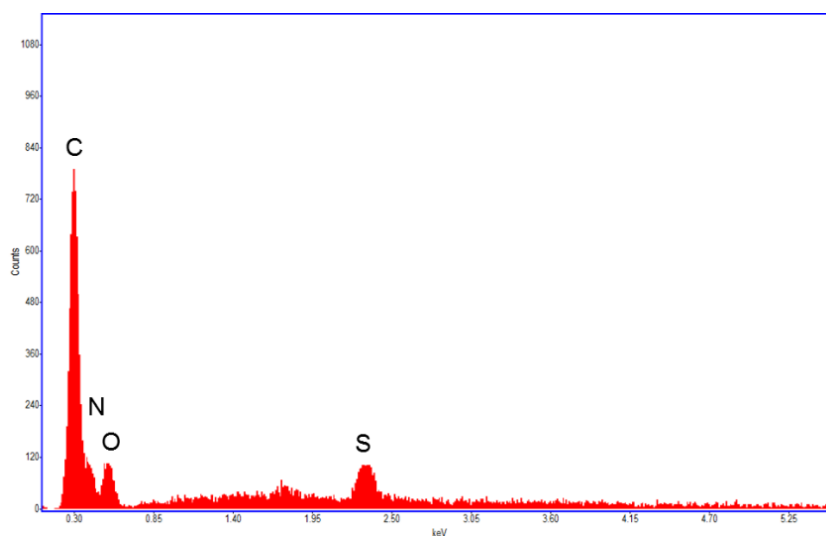


**Figure S22.** EDAX spectrum of **aza-COF-1** showing the presence of C, N, O, and S. The spectrum was obtained after collecting the COF by filtration and washing with water (30 mL  $\times$  3) and acetone (30 mL  $\times$  5). No activation procedure was employed to prior to EDAX analysis. The O and S may come from the trapped O-containing small molecule and the residue of sulfuric acid used in the COF synthesis, respectively.

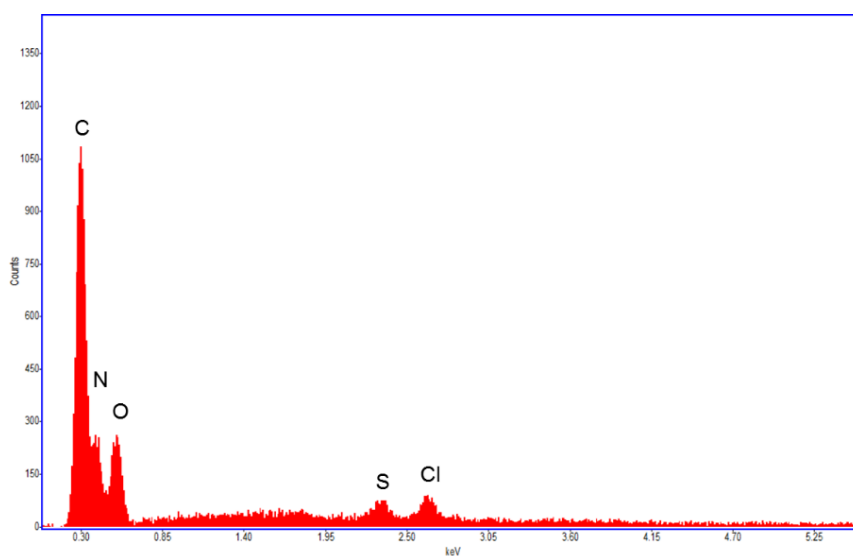


**Figure S23.** EDAX spectrum of **aza-COF-2** showing the presence of C, N, O, S, and Cl. The spectrum was obtained after collecting the COF by filtration and washing with water (30 mL  $\times$  3) and acetone (30 mL  $\times$  5). No activation procedure was employed to prior to EDAX analysis. The O and S may come from the trapped O-containing small molecules and the residue of sulfuric acid used in the COF synthesis, respectively. The trace amount of Cl may come from the ligand starting material: 1,2,4,5-benzenetetramine tetrahydrochloride.

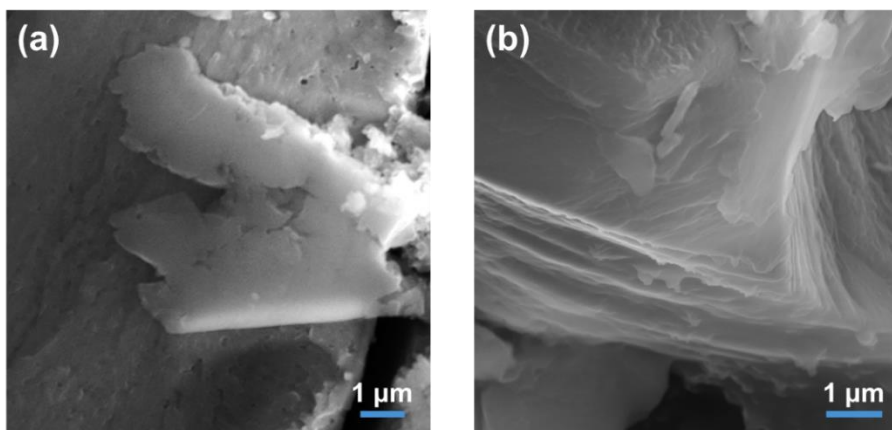


Figure S24. SEM images of (a) aza-COF-1 and (b) aza-COF-2 after being pressed into pellets.

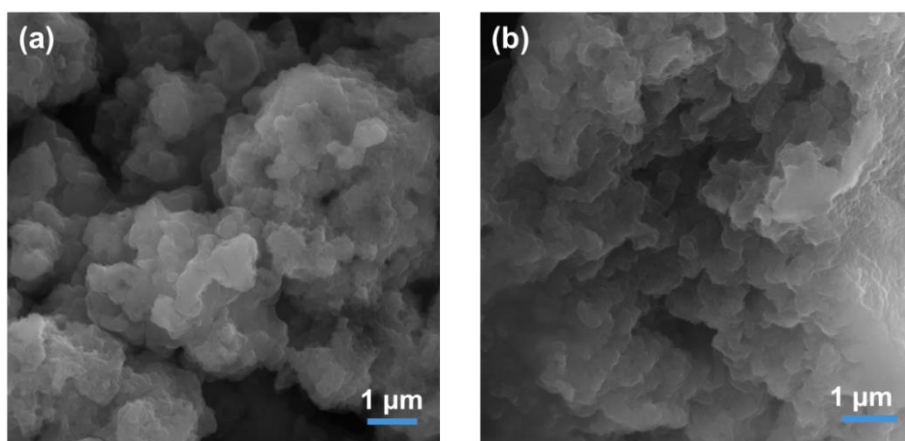


Figure 25. SEM images of acidified materials (a) aza-COF-1<sub>H</sub> and (b) aza-COF-2<sub>H</sub>.

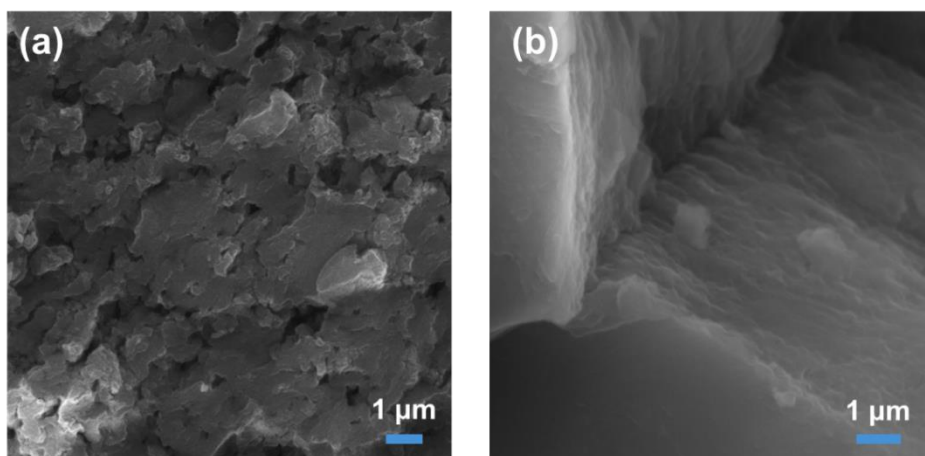
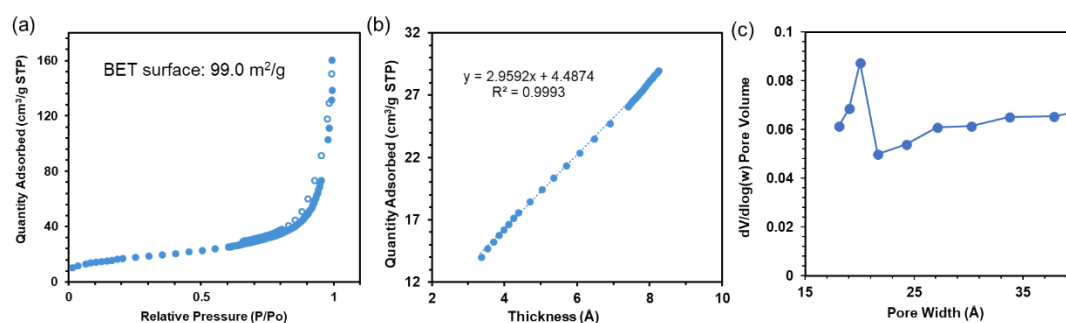


Figure S26. SEM images of (a) aza-COF-1<sub>H</sub> and (b) aza-COF-2<sub>H</sub> after being pressed into pellets.

## 9. Brunauer–Emmett–Teller (BET) Analysis

In order to assess the porosity of aza-fused COFs, gas adsorption measurements were performed on a ASAP Plus 2020 (Micromeritics, Norcross, Georgia) 3FLEX instrument with N<sub>2</sub> at 77K. The samples of **aza-COF-1** and **aza-COF-2** were degassed under vacuum at 150° C from 12 hours. The acidified samples **aza-COF-1<sub>H</sub>** and **aza-COF-2<sub>H</sub>** were degassed under vacuum at 70 °C for 12 hours. For BET calculations, a full isotherm with a fitting range of 0 to 0.3 P/P<sub>0</sub> was used. The BET values for aza-COF-1 was found to be 99.0 m<sup>2</sup> g<sup>-1</sup>, which is 3.8 times higher than the structurally-related analog—C<sub>2</sub>N crystal (BET: 26 m<sup>2</sup> g<sup>-1</sup>, pore-size: ~8 Å) without a treatment at 700 °C.<sup>6</sup> The BET value obtained for **aza-COF-2** was 102.2 m<sup>2</sup> g<sup>-1</sup>. Because aza-COF-2 should have a larger pore size than **aza-COF-1**, a higher BET value would be expected. However, compared with **aza-COF-1**, **aza-COF-2** exhibits lower crystallinity and smaller crystallite size, which can diminish the BET surface area.

The Brunauer-Emmett-Teller (BET) surface areas for **aza-COF-1<sub>H</sub>** and **aza-COF-2<sub>H</sub>** were calculated to be 5.2, 10.9 m<sup>2</sup> g<sup>-1</sup>, respectively.



**Figure S27.** (a) Nitrogen sorption curves (filled circles: adsorption, open circles: desorption, STP=standard temperature pressure) and (b) *t*-Plot for nitrogen adsorbed at 77 K by activated **aza-COF-1**. The BET surface area by the gas adsorption analysis is 99.0 m<sup>2</sup>/g. The internal surface area is 75.7 m<sup>2</sup>/g and the micropore area is 23.3 m<sup>2</sup>/g. (c) pore size distribution of **aza-COF-1**.

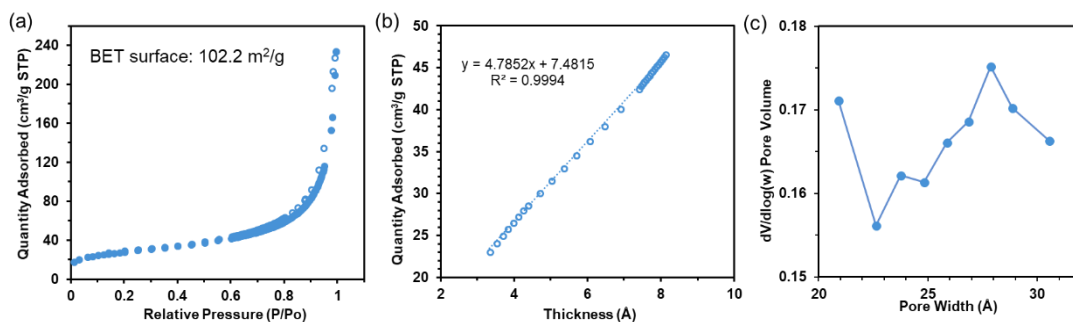


**Figure S28.** (a) Nitrogen sorption curves (filled circles: adsorption, open circles: desorption, STP=standard temperature pressure) and (b) *t*-Plot for nitrogen adsorbed at 77 K by activated **aza-COF-2**. The BET surface area by the gas adsorption analysis is 102.2 m<sup>2</sup>/g. The internal surface area is 74.1 m<sup>2</sup>/g and the micropore area is 28.1 m<sup>2</sup>/g. (c) pore size distribution of **aza-COF-2**.

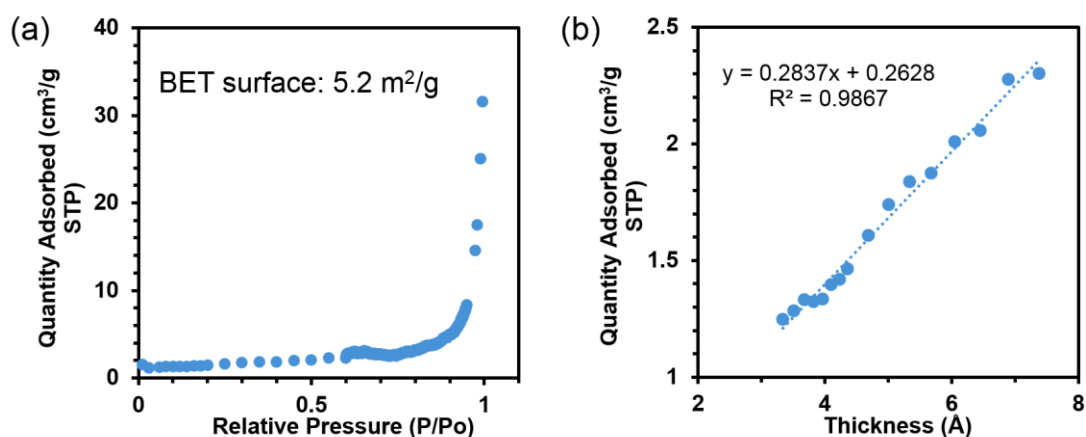


**Figure S29.** (a) Nitrogen adsorption curves (STP=standard temperature pressure) and (b) *t*-Plot for nitrogen adsorbed at 77 K by acidified material **aza-COF-1H**. The BET surface area by the gas adsorption analysis is 5.2 m<sup>2</sup>/g.

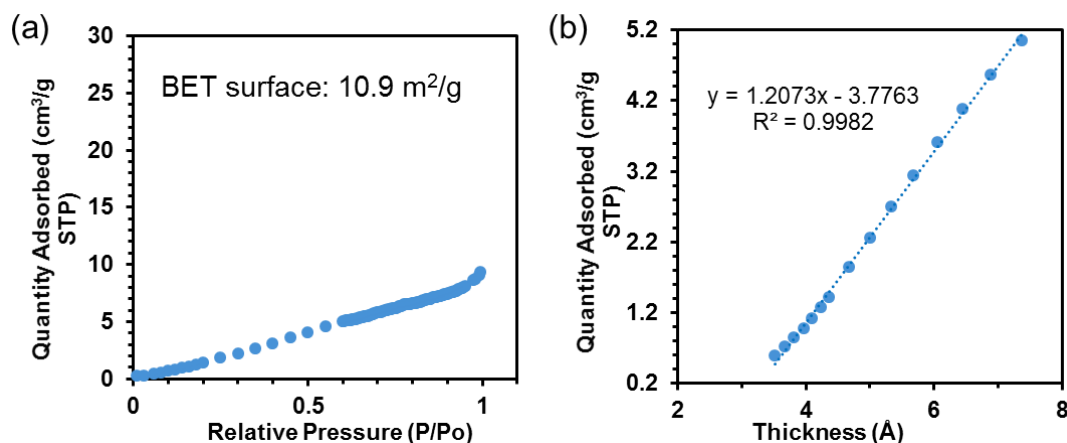


**Figure S30.** (a) Nitrogen adsorption curves (STP=standard temperature pressure) and (b)  $t$ -Plot for nitrogen adsorbed at 77 K by acidified material **aza-COF-2<sub>H</sub>**. The BET surface area by the gas adsorption analysis is 10.9 m<sup>2</sup>/g.

## 10. Thermal Gravimetric Analyses (TGA)

The thermal stability of aza-fused COFs was investigated by thermal gravimetric analysis. Thermogravimetric analysis was performed in a TGA Q50 V5.0 instrument under nitrogen with a heating ramp rate of 20 °C/min. TGA results of **aza-COF-1** reveal a ~4% weight loss before 120 °C (**Figure S31**), due to the loss of small-molecule volatiles (H<sub>2</sub>O, methanol) included in the pores. There is no measurable weight loss until 250 °C, indicating good thermal stability of **aza-COF-1**. A total weight loss of 22% was observed when the temperature went to 500 °C. For **aza-COF-2**, only a weight loss of 2% happened at the temperature of 282 °C due to loss of the small molecules inside the pores and only a total 10% weight loss happened before 500 °C, which again suggests its good thermal stability, as reported in the literature.<sup>S2</sup>

For the acidified materials, there is 8%, 10% weight loss at around 100 °C for **aza-COF-1<sub>H</sub>** and **aza-COF-2<sub>H</sub>**, respectively, which is probably due to the introduction of water molecules during the acidification process. Another observable weight loss occurs at 189 °C and 198 °C, respectively, for **aza-COF-1<sub>H</sub>** and **aza-COF-2<sub>H</sub>**, both of which are much higher than the boiling point of H<sub>3</sub>PO<sub>4</sub> (158 °C). These weight losses happened at lower temperatures when compared pristine COFs (250 °C and 282 °C), demonstrating the presence of a new decomposition process in acidified materials, which can be ascribed to the loss of the phosphate salt resulting from the acidification reaction. The loading of the H<sub>3</sub>PO<sub>4</sub> can be estimated by the weight loss at during the temperature range of 189 to 250 °C and 198 °C to 282 °C, respectively for **aza-COF-1** and **aza-COF-2**.

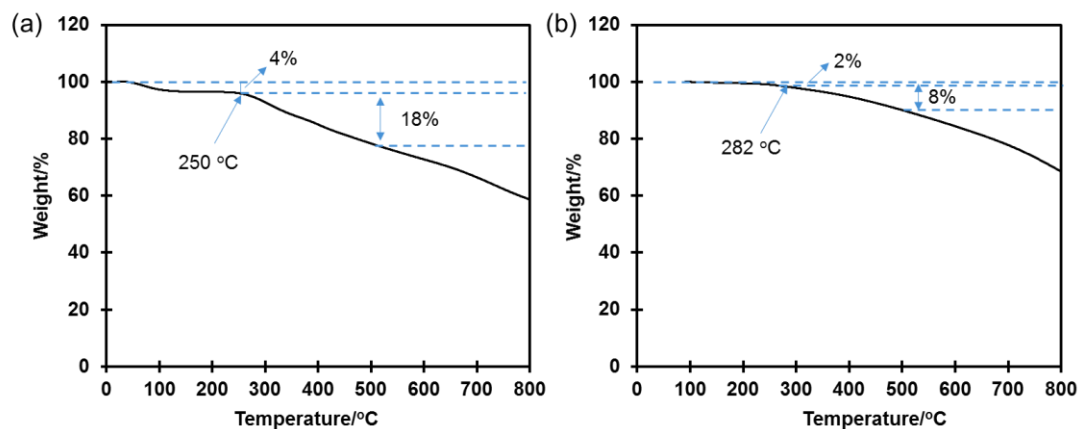


Figure S31. TGA curve of (a) aza-COF-1 and (b) aza-COF-2.

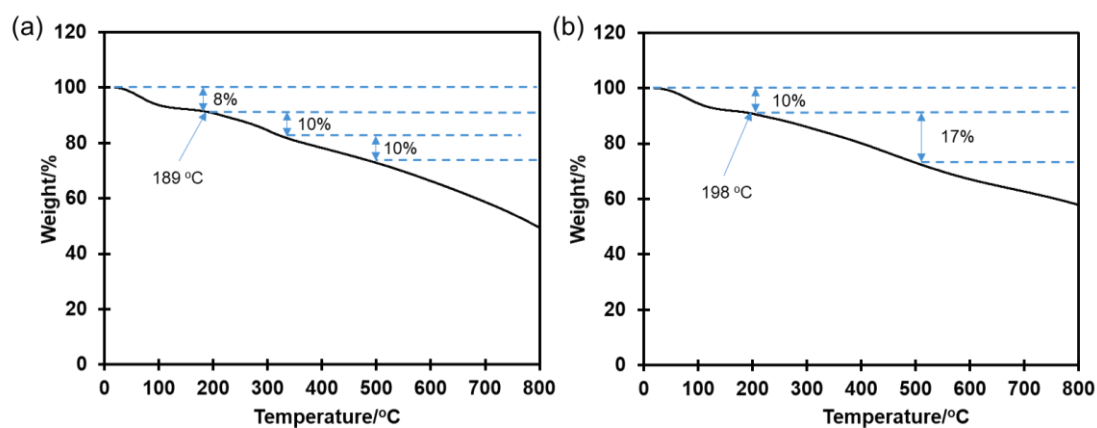


Figure S32. TGA curve of acidified materials aza-COF-1<sub>H</sub> and aza-COF-2<sub>H</sub>.

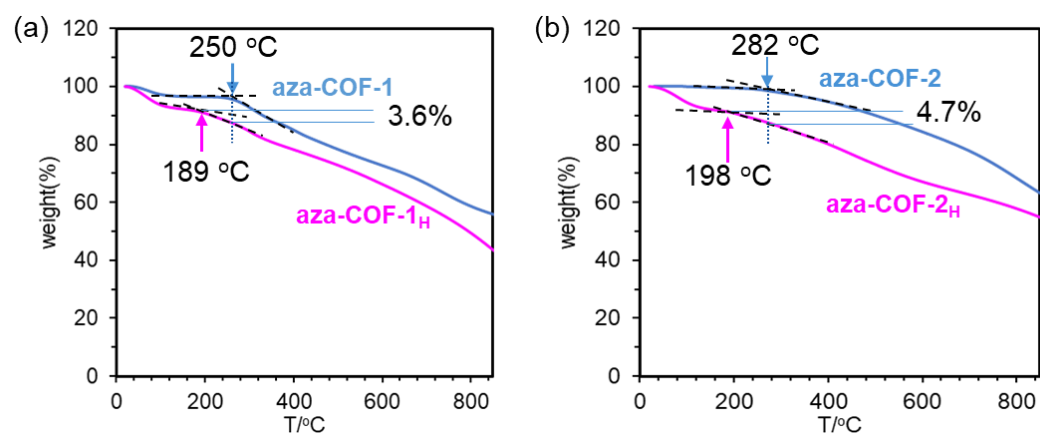


Figure S33. H<sub>3</sub>PO<sub>4</sub> loading of aza-COF-1<sub>H</sub> and aza-COF-2<sub>H</sub> calculated by TGA curves.

## 11. Measurements of Proton Conductivity

Proton conductivities of the COFs were measured using Ivium CompactStat potentiostat B31250. 70 to 80 mg

of COF samples were pressed into a die under 1000 psi for 5 minutes to obtain uniform pellets (1 ~ 2 mm in thickness, 6.0 mm in diameter). The pellet was loaded into custom 2-electrode cell between 25  $\mu\text{m}$  gold foil to enhance contact (**Figure S34a**), and was then inserted in a humidity chamber maintained at 97% RH. The conductivity was subsequently measured at different temperatures. When changing to a new temperature, the sample was allowed to equilibrate for 24 hours. Electrochemical Impedance Spectroscopy (EIS) was performed at AC bias with an amplitude of 100 mV at frequencies from 150 kHz to 1 Hz. Proton conductivity was calculated by the following equation S1:

$$\sigma = L/(RA) \quad \text{S1}$$

where  $\sigma$  is proton conductivity ( $\text{S cm}^{-1}$ ),  $L$  is thickness of the pellet (cm),  $A$  is area of the pellet ( $\text{cm}^2$ ), and  $R$  is the resistance ( $\Omega$ ) of the pellet corresponding to the real  $Z'$  Nyquist plot. The resistance value  $R$  was obtained by fitting the Nyquist plots using the equivalent circuit model as drawn in **Figure S34b**. In this circuit, the capacitance of the COF pellet ( $C$ ), the resistance of the pellet ( $R$ ), and the resistance ascribed from electrode, gold foil and electrical wire ( $R_s$ ) were considered. The capacitance  $C$  is in parallel to the resistance  $R$ , and they are connected in series to  $R_s$ .

The calculated proton conductivity values at different temperatures were fitted to Arrhenius equation shown below (equation S2) to obtain the activation energy  $E_a$  for proton conduction process.

$$\ln(\sigma) = \ln(A_0) - \frac{E_a}{R} \frac{1}{T} \quad \text{S2}$$

In this equation,  $\sigma$  is the proton conductivity measured at temperature  $T$ ,  $A_0$  is a constant,  $R$  is the ideal gas constant.

Although results indicated that there are some small molecule impurities presented in pristine materials after methanol washing for two days, we think these molecules may play only a minor role in the proton conduction. *First*, we had performed the proton conduction of the pristine material under anhydrous condition. The results showed that, compared with the proton conduction values obtained under 97% humidity ( $1.51 \times 10^{-5} \text{ S cm}^{-1}$  and  $8.78 \times 10^{-6} \text{ S cm}^{-1}$  for **aza-COF-1** and **aza-COF-2**, respectively), the proton conduction values of pristine materials under dry conditions are much lower and at  $10^{-8}$  to  $10^{-9} \text{ S cm}^{-1}$  level (**Figure S35**), indicating that the proton conductivity values are strongly dependent on the hydration of the materials rather than other small molecules trapped in the materials. *Second*, the proton conductivity values of pristine materials are 2-3 orders of magnitude smaller than proton conductivity values of the materials that are deliberately acidified, suggesting that the existence of the small molecules inside the materials before the acidification only plays a minor role for the proton transportation.

Grain-boundary resistance can reduce total proton conductivity, which is a commonly found issue for pellets

consisting of small crystallites.<sup>S8</sup> For **aza-COF-1** and **aza-COF-2**, grain boundary effects are resulted from the small crystal size of the materials, as indicated from the SEM and pXRD characterization. This effect can contribute part of the resistance for the proton's long-distance transport. Judging from the Nyquist plots of pellet samples,<sup>S9</sup> it appears that the introduction of  $\text{H}_3\text{PO}_4$  molecules made a contribution to the grain boundary. We think that there can be two possible reasons for the increase in the grain boundary effect through the introduction of  $\text{H}_3\text{PO}_4$  molecules increase grain boundary effect. Firstly, as suggested in the XPS data, the as synthesized materials may contain unreacted amino group on the edges of the crystallites of the materials, because the undesired termination of the condensation reaction. Similar phenomenon has also been reported in a structurally-related material  $\text{C}_2\text{N}$  by Jong-Beom Baek and coworkers.<sup>S6</sup> These amino groups on the edges will be transformed into ammonium ions during the acidification of the materials, leading the materials to be positively charged, which will impair the close contact between vicinal crystallites. Secondly, because the acidification of the materials was performed in the phosphoric acid solution, disordered hydrogen-bonding networks in grain boundaries among the crystallites can be formed considering that unreacted amino/ammonium groups and carbonyl groups can act as hydrogen bonding donors/acceptors. The formation of the disordered hydrogen-bonding networks again will result in larger grain-boundary.<sup>S8</sup>

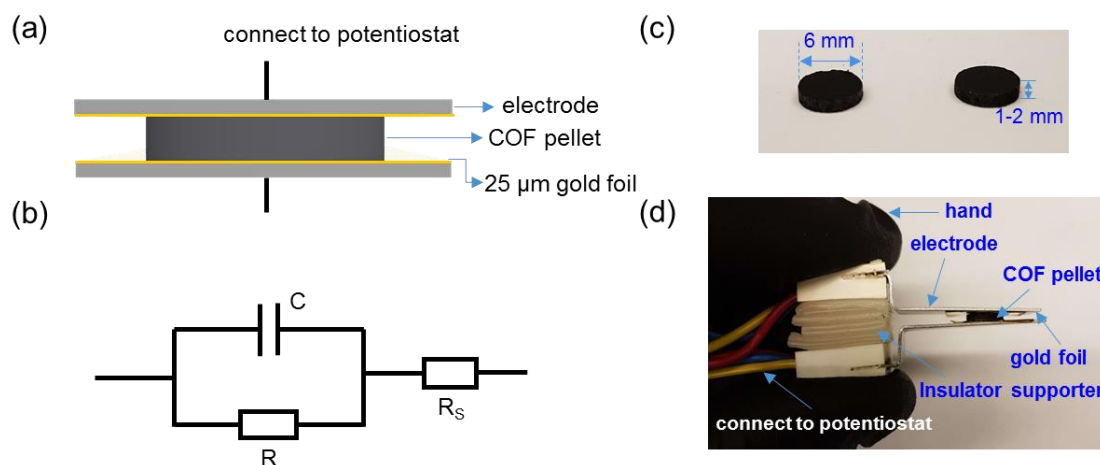


**Figure S34.** (a) Scheme representation of 2-electrode cell sandwiching the pallet of COFs used for proton conductivity measurements. (b) Equivalent circuit model used for the fitting the Nyquist plots. (c) Digital photographs of COF pellets. (d) Digital photograph of the 2-electrode cell used for the proton conductivity measurements.

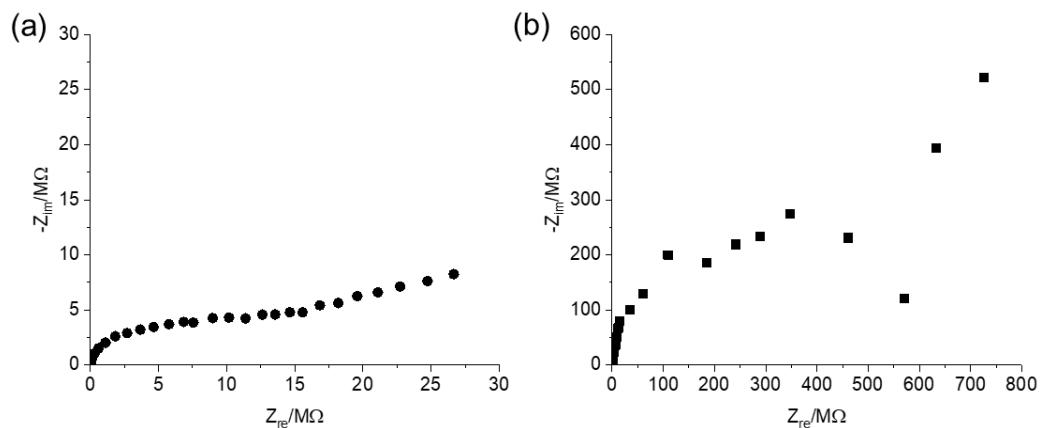


**Figure S35.** Nyquist plots (150 kHz-1 Hz, amplitude: 100 mV) of (a) **aza-COF-1** and (b) **aza-COF-2** measured at under anhydrous conditions at 323 K.

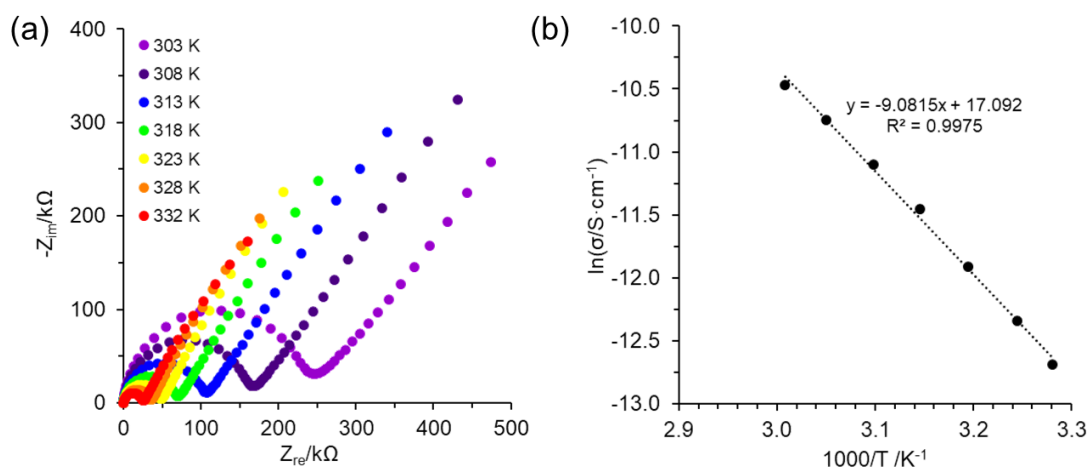


**Figure S36.** Nyquist plots (150 kHz-1 Hz, amplitude: 100 mV) of **aza-COF-1** measured at different temperatures under 97% RH showing the temperature dependence of proton conductivities. (b) Arrhenius plot for **aza-COF-1** at different temperature. Dots are experimental data; lines are curve-fitting results.

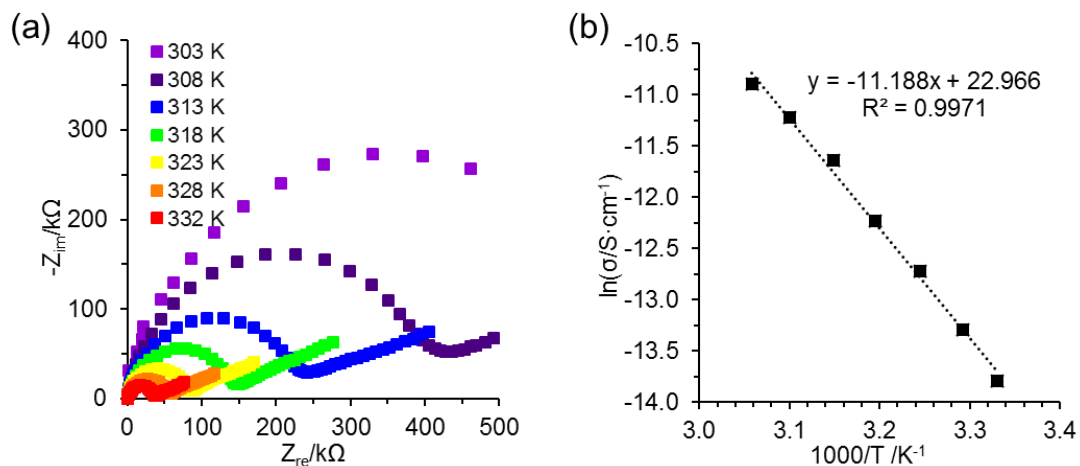


**Figure S37.** Nyquist plots (150 kHz-1 Hz, amplitude: 100 mV) of **aza-COF-2** measured at different temperatures under 97% RH showing the temperature dependence of proton conductivities. (b) Arrhenius plot for **aza-COF-2** at different temperature. Dots are experimental data; lines are curve-fitting results.

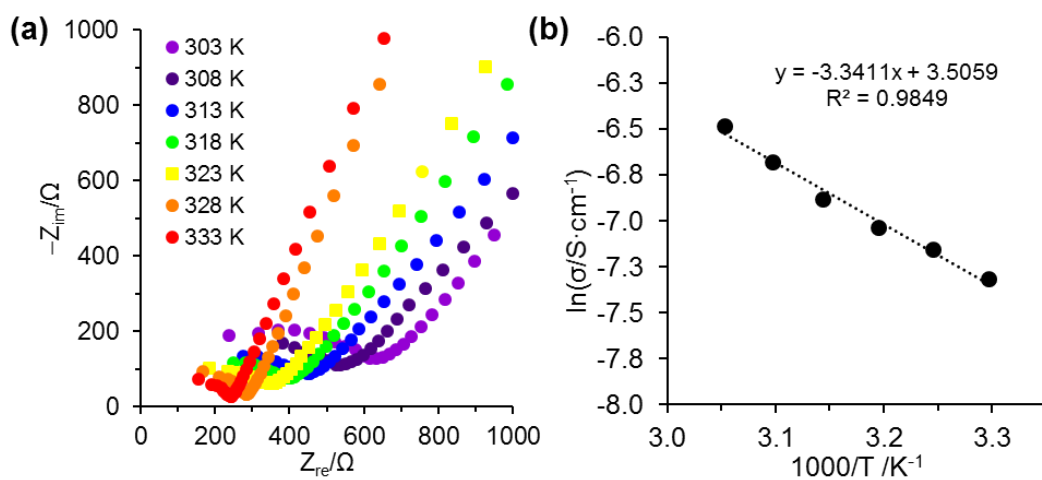


**Figure S38.** Nyquist plots (150 kHz-1 Hz, amplitude: 100 mV) of acidified materials **aza-COF-1H** measured at different temperatures under 97% RH showing the temperature dependence of proton conductivities. (b) Arrhenius plot for materials **aza-COF-1H** at different temperature. Dots are experimental data; lines are curve-fitting results.

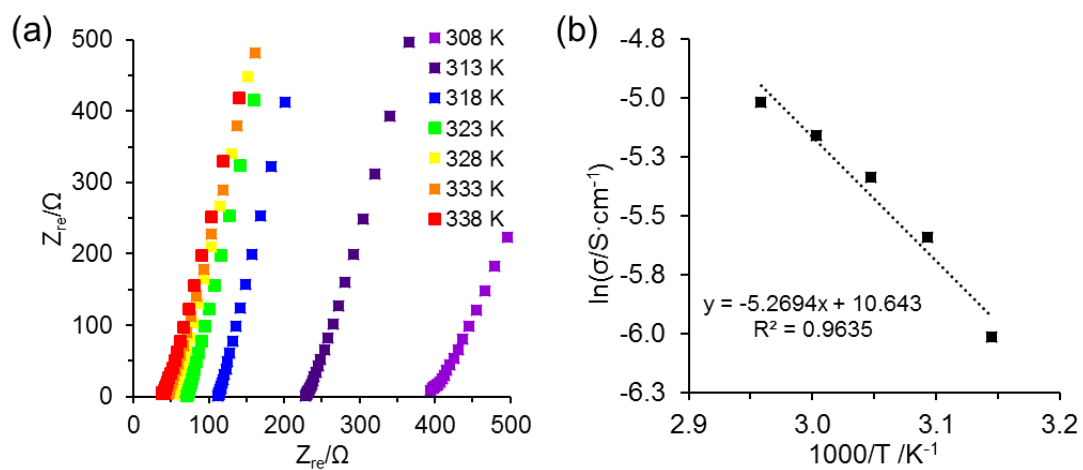


**Figure S39.** Nyquist plots (150 kHz-1 Hz, amplitude: 100 mV) of acidified materials **aza-COF-2<sub>H</sub>** measured at different temperatures under 97% RH showing the temperature dependence of proton conductivities. (b) Arrhenius plot for materials **aza-COF-2<sub>H</sub>** at different temperature. Dots are experimental data; lines are curve-fitting results.

## 12. Summary of the COFs Based Proton Conducting Materials

**Table S3.** List of proton conducting material based on COFs.

COFs	Type of the linkages in COFs	Proton conductivity (S/cm)	condition	Ref
PA@TP-Stb	$\beta$ -ketoenamine	$2.3 \times 10^{-5}$	332 K, 98% RH	S10
PA@TP-Azo	$\beta$ -ketoenamine	$9.9 \times 10^{-4}$	332 K, 98% RH	S10
im@TPB-DMTP- COF	imine	$1.79 \times 10^{-3}$	398 K, anhydrous	S11
trz@TPB-DMTP- COF	imine	$7.0 \times 10^{-4}$	398 K, anhydrous	S11
EB-COF:Br	$\beta$ -ketoenamine	$2.82 \times 10^{-6}$	298 K, 97% RH	S12
EB-COF:PW <sub>12</sub>	$\beta$ -ketoenamine	$3.32 \times 10^{-3}$	298 K, 97% RH	S12
TpPa-SO <sub>3</sub> H	$\beta$ -ketoenamine	$1.7 \times 10^{-5}$	393 K, anhydrous	S13
Phytic@TpPa- (SO <sub>3</sub> H-Py)	$\beta$ -ketoenamine	$5 \times 10^{-4}$	393 K, anhydrous	S13
NUS-9 (R)	$\beta$ -ketoenamine	$1.24 \times 10^{-2}$	298 K, 97% RH	S14
NUS-10 (R)	$\beta$ -ketoenamine	$3.96 \times 10^{-2}$	298 K, 97% RH	S14
PA@TpBpy-ST	$\beta$ -ketoenamine	$1.98 \times 10^{-3}$	393 K, anhydrous	S15
PA@TpBpy-MC	$\beta$ -ketoenamine	$2.5 \times 10^{-3}$	393 K, anhydrous	S15
RT-COF-1	imine	$1.83 \times 10^{-5}$	313 K, 100% RH	S16
RT-COF-1AC	imine	$1.07 \times 10^{-4}$	313 K, 100% RH	S16
RT-COF-1AcB	imine	$5.25 \times 10^{-4}$	313 K, 100% RH	S16
LiCl@RT-COF-1	imine	$6.45 \times 10^{-3}$	313 K, 100% RH	S16
PTSA@TpAzo	$\beta$ -ketoenamine	$7.8 \times 10^{-2}$	353 K, 95% RH	S17
aza-COF-1	aromatic pyrazine linkage	$1.51 \times 10^{-5}$	323 K, 97%	<i>This work</i>
aza-COF-2		$8.78 \times 10^{-6}$	323 K, 97%	<i>This work</i>
aza-COF-1 <sub>H</sub>		$1.23 \times 10^{-3}$	323 K, 97%	<i>This work</i>
aza-COF-2 <sub>H</sub>		$4.80 \times 10^{-3}$	323 K, 97%	<i>This work</i>

### 13. References

- S1. Chen, L.; Kim, J.; Ishizuka, T.; Honsho, Y.; Saeki, A.; Seki, S.; Ihee, H.; Jiang, D. Noncovalently Nettle, Photoconductive Sheets with Extremely High Carrier Mobility and Conduction Anisotropy from Triphenylene-Fused Metal Trigon Conjugates. *J. Am. Chem. Soc.* **2009**, *131*, 7287–7292.
- S2. Briega-Martos, V.; Ferre-Vilaplana, A.; de la Peña, A.; Segura, J. L.; Zamora, F.; Feliu, J. M.; Herrero, E. An Aza-Fused  $\Pi$ -Conjugated Microporous Framework Catalyzes the Production of Hydrogen Peroxide. *ACS Catalysis* **2017**, *7*, 1015–1024.
- S3. Guo, J.; Xu, Y.; Jin, S.; Chen, L.; Kaji, T.; Honsho, Y.; Addicoat, M. A.; Kim, J.; Saeki, A.; Ihee, H.; Seki, S.; Irle, S.; Hiramoto, M.; Gao, J.; Jiang, D. Conjugated Organic Framework with Three-Dimensionally Ordered Stable Structure and Delocalized  $\Pi$  Clouds. *Nat. Commun.* **2013**, *4*, 2736.
- S4. Kou, Y.; Xu, Y.; Guo, Z.; Jiang, D. Supercapacitive Energy Storage and Electric Power Supply Using an Aza-Fused  $\pi$ -Conjugated Microporous Framework. *Angew. Chem. Int. Ed.* **2011**, *50*, 8753–8757.
- S5. Marco, A. B.; Cortizo-Lacalle, D.; Perez-Miqueo, I.; Valenti, G.; Boni, A.; Plas, J.; Strutynski, K.; De Feyter, S.; Paolucci, F.; Montes, M.; Khlobystov, A. N.; Melle-Franco, M.; Mateo-Alonso, A. Twisted Aromatic Frameworks: Readily Exfoliable and Solution-Processable Two-Dimensional Conjugated Microporous Polymers. *Angew. Chem. Int. Ed.* **2017**, *56*, 6946–6951.
- S6. Mahmood, J.; Lee, E. K.; Jung, M.; Shin, D.; Jeon, I. Y.; Jung, S. M.; Choi, H. J.; Seo, J. M.; Bae, S. Y.; Sohn, S. D.; Park, N.; Oh, J. H.; Shin, H. J.; Baek, J. B. Nitrogenated Holey Two-Dimensional Structures. *Nat. Commun.* **2015**, *6*, 6486.
- S7. Wang, X.; Maeda, K.; Thomas, A.; Takanabe, K.; Xin, G.; Carlsson, J. M.; Domen, K.; Antonietti, M. A Metal-Free Polymeric Photocatalyst for Hydrogen Production from Water under Visible Light. *Nat. Mater.* **2009**, *8*, 76–80.
- S8. Ono, K.; Ishizaki, M.; Kanaizuka, K.; Togashi, T.; Yamada, T.; Kitagawa, H.; Kurihara, M. Grain-Boundary-Free Super-Proton Conduction of a Solution-Processed Prussian-Blue Nanoparticle Film. *Angew. Chem. Int. Ed.* **2017**, *56*, 5531–5535.
- S9. Yamazaki, Y.; Hernandez-Sanchez, R.; Haile, S. M. High Total Proton Conductivity in Large-Grained Yttrium-Doped Barium Zirconate. *Chem. Mater.* **2009**, *21*, 2755–2762.
- S10. Chandra, S.; Kundu, T.; Kandambeth, S.; Babarao, R.; Marathe, Y.; Kunjir, S. M.; Banerjee, R. Phosphoric Acid Loaded Azo ( $=N=N=$ ) Based Covalent Organic Framework for Proton Conduction. *J. Am. Chem. Soc.* **2014**, *136*, 6570–6573.
- S11. Xu, H.; Tao, S.; Jiang, D. Proton Conduction in Crystalline and Porous Covalent Organic Frameworks. *Nat. Mater.* **2016**, *15*, 722–726.
- S12. Ma, H.; Liu, B.; Li, B.; Zhang, L.; Li, Y. G.; Tan, H. Q.; Zang, H. Y.; Zhu, G. Cationic Covalent Organic Frameworks: A Simple Platform of Anionic Exchange for Porosity Tuning and Proton Conduction. *J. Am. Chem. Soc.* **2016**, *138*, 5897–5903.
- S13. Chandra, S.; Kundu, T.; Dey, K.; Addicoat, M.; Heine, T.; Banerjee, R. Interplaying Intrinsic and Extrinsic Proton Conductivities in Covalent Organic Frameworks. *Chem. Mater.* **2016**, *28*, 1489–1494.
- S14. Peng, Y.; Xu, G.; Hu, Z.; Cheng, Y.; Chi, C.; Yuan, D.; Cheng, H.; Zhao, D. Mechanoassisted Synthesis of Sulfonated Covalent Organic Frameworks with High Intrinsic Proton Conductivity. *ACS Appl. Mater. Interfaces* **2016**, *8*, 18505–18512.
- S15. Shinde, D. B.; Aiyappa, H. B.; Bhadra, M.; Biswal, B. P.; Wadge, P.; Kandambeth, S.; Garai, B.; Kundu, T.; Kurungot, S.; Banerjee, R. A Mechanochemically Synthesized Covalent Organic Framework as a Proton-Conducting Solid Electrolyte. *J. Mater. Chem. A* **2016**, *4*, 2682–2690.
- S16. Montoro, C.; Rodriguez-San-Miguel, D.; Polo, E.; Escudero-Cid, R.; Ruiz-Gonzalez, M. L.; Navarro, J. A. R.; Ocon, P.; Zamora, F. Ionic Conductivity and Potential Application for Fuel Cell of a Modified Imine-Based Covalent Organic Framework. *J. Am. Chem. Soc.* **2017**, *139*, 10079–10086.
- S17. Sasmal, H. S.; Aiyappa, H. B.; Bhange, S. N.; Karak, S.; Halder, A.; Kurungot, S.; Banerjee, R. Superprotonic Conductivity in Flexible Porous Covalent Organic Framework Membranes. *Angew. Chem. Int. Ed.* **2018**, *57*, 10894–10898.